

Powder bed properties modelling and 3D thermo-mechanical simulation of the additive manufacturing Electron Beam Melting process

Original

Powder bed properties modelling and 3D thermo-mechanical simulation of the additive manufacturing Electron Beam Melting process / Galati, M.; Snis, A.; Iuliano, L.. - In: ADDITIVE MANUFACTURING. - ISSN 2214-8604. - ELETTRONICO. - 30:(2019), p. 100897. [10.1016/j.addma.2019.100897]

Availability:

This version is available at: 11583/2770679 since: 2019-12-02T10:16:27Z

Publisher:

Elsevier B.V.

Published

DOI:10.1016/j.addma.2019.100897

Terms of use:

This article is made available under terms and conditions as specified in the corresponding bibliographic description in the repository

Publisher copyright

Elsevier postprint/Author's Accepted Manuscript

© 2019. This manuscript version is made available under the CC-BY-NC-ND 4.0 license
<http://creativecommons.org/licenses/by-nc-nd/4.0/>. The final authenticated version is available online at:
<http://dx.doi.org/10.1016/j.addma.2019.100897>

(Article begins on next page)

Powder bed properties modelling and 3D thermo-mechanical simulation of the additive manufacturing Electron Beam Melting process

Manuela Galati^{1*}, Anders Snis², Luca Iuliano¹

¹Integrated Additive Manufacturing Center (IAM) - Department of Management and Production Engineering (DIGEP)-Politecnico di Torino, Torino, Italy

²Arcam AB, Krokslätts Fabriker 27A, SE-431 37 Mölndal, Sweden

Manuela Galati (*Corresponding Author*)

Politecnico di Torino, Department of Management and Production Engineering (DIGEP)

Corso Duca Degli Abruzzi, 24 - 10129 Torino, Italy

email: manuela.galati@polito.it

phone: +39 011 090.7280

fax: +39 011 090.7299

Abstract

In this work, an improved but still rather simple computational analysis is presented for a more detailed prediction of Electron Beam Melting (EBM) process outcomes. A fully coupled thermomechanical analysis is developed in which nonlinearities due to the variation of material properties when the material melts are included. A new analytical approach is developed to emulate the volume variation of the powder bed during heating and melting. Particularly, the expansion of the powder particles and the porosity reduction within the powder bed are considered simultaneously. The thermal expansion and the shrinkage of solid material during heating and cooling and the stress formation within the solid material are also modelled. The model can predict the geometrical transformation of the powder into solid material in an efficient way. A comparison between experimental and simulated cross-sectional areas of melted single lines is presented. Both continuous line melting and fractional line melting, multi beam melting, are considered. The model shows a good ability to provide consistent and accurate forecasts. The maximum deviations between experimental and numerical results are approximately 15% for the height and 5% for the width of the melted lines, respectively. A comparison with a pure thermal model is also included, and benefits and differences between the two models are discussed.

Keywords

EBM process modelling; powder bed shrinkage; powder mechanical properties; experimental validation; thermomechanical modelling.

1. Introduction

Electron Beam Melting (EBM) is a metal powder bed fusion (PBF) additive manufacturing (AM) process in which an electron beam (EB) is used as heating source [1]. Unlike other metal powder bed AM processes, EBM is used for mass production in several fields. Especially for materials for which traditional manufacturing technologies have problems related to high melting temperatures and high oxygen affinity [2]. For instance, titanium [3-8] and its alloys [7] are of particular interest for EBM.

The EBM process consists of different steps. After the powder layer distribution and before the melting phase, the powder bed is preheated uniformly by a number of beam passages at high beam current and high scan speed to increase temperature [9], e.g. up to 700°- 800° C for Ti6Al4V and up to 1050° for Ti48Al2Cr2Nb. The aim of the preheating step is mainly to pre-sinter the powder particles. Thus, the spreading of the powder during the melting phase is avoided [10] and the thermal gradients between the melting area and the surrounding are decreased. During the melting phase, the contour of the part is typically melted using a MultiBeamTM strategy [11, 12], while the inner area is

melted using a continuous line hatching mode [12]. After the melting phase, an additional step, called postheating takes place [13]. In this step, the layer can be either cooled down or further heated depending on the total amount of energy supplied during the previous steps. Since the sintered powder has a certain strength [14], parts can be easily nested and the number of down-facing surfaces that require support structures during the process is reduced [15]. The whole process takes place under vacuum. The different heating steps and the vacuum environment assure high temperatures and low thermal gradients during the process. For this reason, EBM-processed parts can be used without any stress-relieving operation [16].

Since the EBM technology is an AM technology used for mass production for aerospace and medical applications [15], the technology is attracting a lot of research activities. Particularly, EBM process optimisation is of interest [17]. Today optimisation of the EBM process parameters is mostly based on experimental trial and error methods. However, to enhance the reliability of the process, several studies have been focused on developing models with different levels of complexity [10]. Due to the significant high computational costs and limited access to commercial codes, many researchers [18-28] are considering the finite element (FE) methodology as the most practical choice to simulate the EBM process. Most of the FE models presented in the literature have considered thermal aspects only [18-25]. Thermomechanical models have been introduced [27, 28], but only for considering thermal stress and part distortion that occur during the cooling phase. Riedlbauer, Steinmann and Mergheim [26] studied the performance of two different algorithms for solving a simplified mechanical problem in which e.g. latent heat effects and powder density changes were not included. Such effects need to be accounted for when predicting the size of the melt zone and the subsequent formation of melt tracks. In addition, due to the lack and the problems of in-situ monitoring [25], experimental validations are seldom performed. Instead, the numerical models were validated using measurements from Selective Laser Melting, Selective Laser Sintering or Electron Beam Welding processes [20, 27, 28] or only numerically verified [26]. In [20, 28], the difference between the calculated melt pool widths and the experimental ones fabricated by EBM was up to 50%. To reduce the differences between numerical and experimental outcomes, tuning coefficients were used to calibrate the models. Some of these coefficients have been used to emulate for instance the absorption efficiency of the EB energy source [19, 24]. Although the match between experimental and numerical values was improved, the applicability of these models may be limited to certain materials, powder fractions and process settings only.

In this work, an improved but still rather simple computational analysis is presented for a more detailed prediction of EBM process outcomes. A fully coupled thermomechanical analysis is developed in which nonlinearities due to the variation of material properties when the material melts

are included. The thermal expansion and the shrinkage of solid material during heating and cooling are modelled together with the stress fields formed within the solid material. A new analytical formulation is introduced to model the powder bed behaviour during the heating. Additionally, the porosity reduction and the shrinkage of the powder layer during the melting phase are considered simultaneously. The model is validated by comparing experimental and numerical results for Ti6Al4V. Single lines are melted using both continuous and MultiBeamTM strategies. To evaluate the accuracy of the model, the calculated widths, heights and areas of the melted lines cross-sections are compared with micrographs. A comparison, in terms of temperature distribution, melt pool geometry and time of calculations between the thermomechanical model and a pure thermal model are also presented.

2. Modelling

2.1 Thermal model

The numerical modelling has been based on the fundamentals presented in [29], in which a 3D local scale model of the EBM process was used to consider thermal aspects. The thermal model used a novel analytical model for the energy source and another model for emulating the thermal properties of the powder. Monte Carlo simulations were used to develop the analytical energy source that mimics the EB impact on the powder surface. From these simulations, it becomes possible to replace the beam size with an effective beam diameter D_E that mimics the electron distribution at the surface. On the powder surface, the model of the energy source was defined as a uniform heat distribution on a circular area in which a coefficient η , including D_E , was used to couple the electron beam size with the uniform heat source. The powder bed was modelled as a continuum, in which the thermal properties depended on the average size of the particles and the powder bed porosity ϕ . The analytical models for both the powder and the solid material were developed from the corresponding temperature-dependent bulk material properties [29]. The thermal transfer in the powder bed considered both thermal radiation in the pores and the heat transfer through the powder necks that are formed during the preheating [29]. The specific heat and the latent heat of fusion of the powder bed were assumed to be equal to those of the solid bulk material [19, 20, 30, 31].

For each node of the model, a variable MAT_ID was used to indicate the material state. The material state of the powder bed was defined as "powder" (MAT_ID=0) before the melting point and as "bulk" (MAT_ID=1) after the melting point has been reached. The bulk material state (MAT_ID=1) was used for both the liquid state and for all the solid material in the model. For a detailed description of the basic thermal model, please see [29].

2.2 Coupled thermal and mechanical model

To consider a fully coupled thermal and mechanical analysis, the pure thermal model has been updated with temperature and material state-dependent mechanical properties. The following material properties have been modified or added to the model:

- Density
- Coefficient of linear thermal expansion (CTE)
- Young modulus
- Poisson ratio
- Annealing temperature

From a macroscopic point of view and for the typical powder size distribution for the EBM process, the apparent density of the preheated powder bed can be approximated to 68% of the solid material [23]. The porosity ϕ is then equal to 0.32 [32]. This means that the mass of a volume V_0 in which the powder is contained is equal to 68% of the corresponding solid material.

Considering the single powder particle, during the heating phase, the particles increase their temperature. An increase in temperature leads to an increase in the volume of the particle up to complete melting. During the heating, the expansion of each particle will fill partially the porosity of the powder bed. After the melting point, however, the melted particles should fill completely the residual porosity of the powder bed, to obtain a fully dense material.

To model the behaviour of the powder bed during heating, at the macroscopic scale, a balance between the following two phenomena should be considered: 1) the thermal expansion of the single powder particles; 2) the changing of the porosity of the powder bed. As the powder bed has been modelled as a continuum, the powder bed proprieties are obtained under the following hypotheses.

- no thermal stress is generated in the powder. This means that thermal expansion within the powder bed is completely free up to the melting point. Therefore, the particles can expand their volume freely and the heat transfer by conduction increases.
- in any transition phase, the total mass is preserved. This means that the mass in a specified volume does not change when the particles are expanding or shrinking.

The first corollary of the hypotheses allows for defining the volume variation by means of two contributions. The first one represents the increase of the volume due to the thermal expansion of the powder particles during the heating. The second one describes the volume lost due to the reduction of the distance between the powder particles and the melting of the powder that in turn decrease the porosity of the powder bed.

$$\delta V = \delta V_1 + \delta V_2 = (1 - \varphi(T))V\alpha_{BULK}\delta T - \varphi(T)V \quad (1)$$

Here V is the volume where the powder is contained, T defines the variable temperature, $\varphi(T)$ is the temperature-dependent porosity and α_{BULK} is the thermal volumetric temperature expansion coefficient of the bulk material. The term $(1 - \varphi(T))V$ represents the temperature-dependent quantity of the total volume occupied by powder. It should be noted that the powder particles are expected to expand their dimensions according to the bulk material properties.

Considering that Equation 1 states a total volume variation due to thermal effects, it is possible to define a pseudo volumetric temperature expansion coefficient $\tilde{\alpha}_V$ that emulates the powder bed behaviour below the solidus temperature.

$$\tilde{\alpha}_V = (1 - \varphi(T))\alpha_{BULK} - \frac{\varphi(T)}{\delta T}$$

Here $\varphi(T)$ is defined as a linear function for which the porosity is equal to 0.32 at the preheating temperature and zero at the melting temperature. Because of that, the density of the powder bed which was already defined as a variable of the material state has been modelled to satisfy the second hypothesis. Therefore, the density of the powder is modelled as a linear function as well. The initial density of the preheated powder bed is set equal to the apparent density, while the density of the powder bed at the melting point is calculated to have the same mass as the powder but in a smaller volume. This volume is calculated by assuming zero porosity at the solidus temperature. Consequently, the density of the powder bed at the melting temperature is somewhat higher than the corresponding density of the bulk material at the same temperature. In the model, $\tilde{\alpha}_V$ has been implemented as a mechanical property of the powder material. The Young's modulus has been expressed as a function of the porosity considering the findings presented in [33, 34], while Poisson's ratio has been assumed to be temperature-dependent only [27, 35]. The annealing temperature has been set equal to the solidus temperature, $T_{Solidus}$, to satisfy the first hypothesis. Figure 1 depicts the effect on a powder bed of Ti6Al4V when the presented formulations have been implemented. While the beam is heating the powder, the volume of the powder bed slightly reduces. When the temperature achieves the melting point the material state changes from powder to bulk (blue to red in Figure 1), and above the melting point, a pure thermal expansion takes place. Gradually, even the surrounding material is affected by the heat transfer and properties are updated according to the temperature.

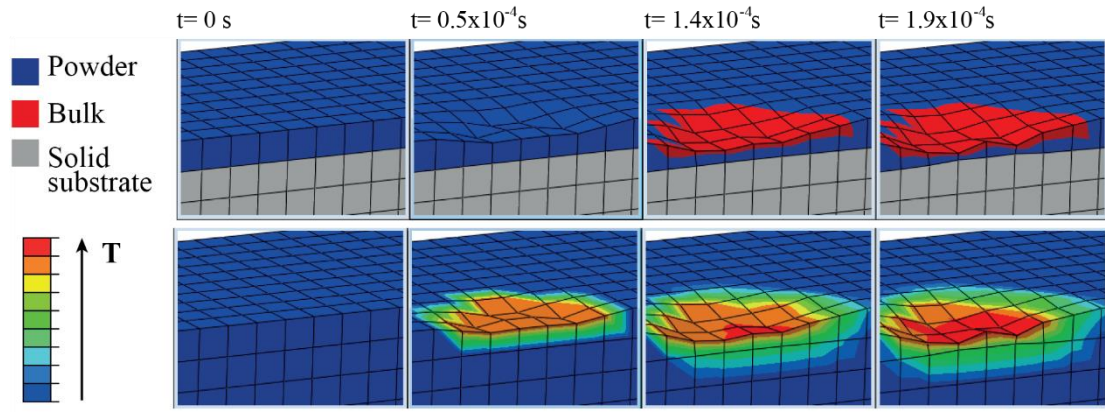


Figure 1 The modelled macroscopic effects obtained when heating the powder bed with the EB source. In the upper figure, the value of the material state variable is displayed, whereas in the lower figure the corresponding temperature distributions are shown. The grey part represents the solid substrate previously melted.

As for the pure thermal model, the material properties from powder to bulk material are updated according to the material state variable MAT_ID [29]. The update of MAT_ID works as shown in Figure 2.

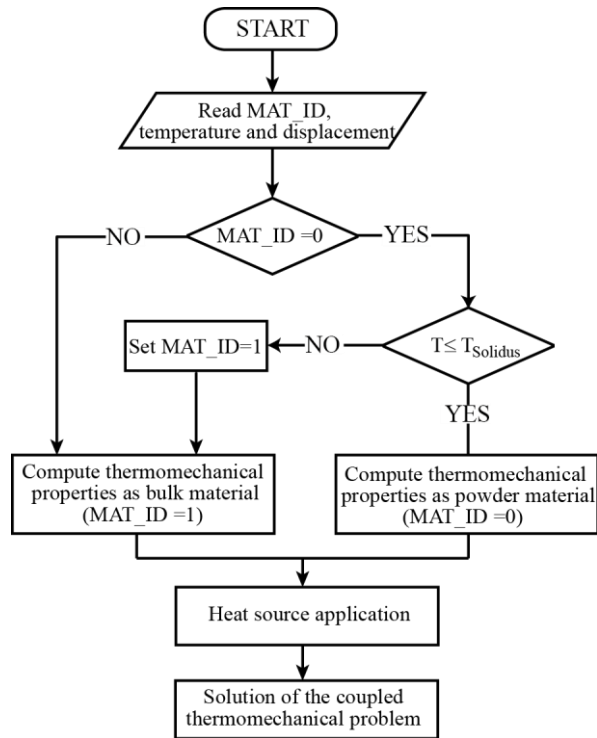


Figure 2 Workflow of the management of the material properties

3. Numerical model implementation

3.1 Model configuration

The overall modelling strategy reproduced the EBM process by simulating the melting of single lines. Both continuous line melting and MultiBeamTM melting were considered. The FE fully coupled thermomechanical model was implemented in Abaqus/Standard. The model consisted of a substrate

of solid bulk material and one single layer of powder material. The thickness of the solid substrate is 9.95 mm and, to reduce the calculation time, 2D shell elements were used at the bottom whereas 3D solid elements were used elsewhere. The thickness property of the shell elements was set to 9.4 mm. The different regions between the elements are fused together by a tie constraint [36]. In the proximity of the heat flux, a fine element size equal to 0.050 mm was used (Cf. Figure 3). The initial temperature was set equal to the preheating temperature $T_{preheat}$. The same temperature was used for the adiabatic boundary conditions on all surfaces except the top surface. On the top surface, heat losses due to radiation were computed using the user code FILM. The melting of a single line was simulated by moving the EB source along the x_1 axis (Cf. Figure 3) at a fixed scan speed for a predefined distance. A specific user code (DFLUX) controlled the EB movement. The material properties, as updated according to the workflow in Figure 2, are managed by the user codes UMATH and USDFLD. As far as the mechanical boundary condition was concerned, all the geometric degrees of freedom on the bottom of the model have been constrained to simulate the adhesion to the build plate. Figure 3 depicts the general model with the heat load and the boundary conditions. The overall dimensions of the model in Figure 3 are $4 \times 5 \times 0.60 \text{ mm}^3$.

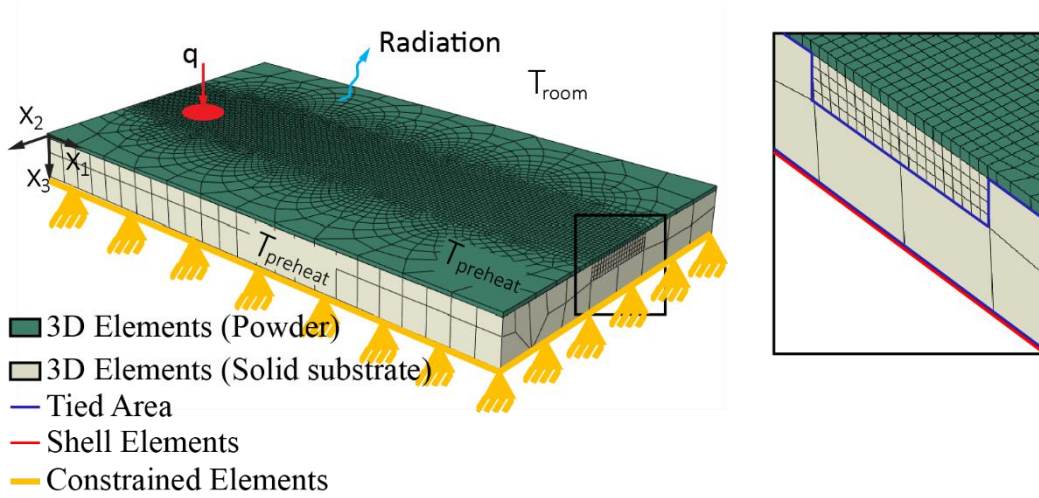


Figure 3 FE model configuration and boundary conditions

The thermal energy balance problem was solved fully coupled with the mechanical problem as a function of both space and time. Latent enthalpy effects were included by calculating, for each time step, the fraction of liquid in the system. Then, the energy density was updated with the amount of the latent heat of fusion as well. The structural analysis for the mechanical problem considered that the total strain tensor ε is a superposition of the three contributions: elastic strain, plastic strain and thermal strain, respectively. The approach adopted followed the mechanical definitions reported in [35].

The material Ti6Al4V was considered for the analysis. The bulk material properties were collected from [28, 31, 35, 37-39]. In Table 1, a summary of the data used to calculate the powder material properties is presented.

Material Properties	
Density at 293 K [kg/mm ³]	3.93
Solidus Temperature [K]	1,873
Liquidus Temperature [K]	1,928
Average particle size [μm]	75

Table 1. Material properties.

3.2 Model validation

The validation of the model has been carried out by comparing experimental and numerical results. Several single melted lines have been simulated by varying the scanning strategy and the scan speed. The inputs for the simulation are listed in Table 2. The parameters are a part of the full factorial DOE plan used for the validation of the pure thermal model [40].

Simulation Parameters		
T _{preheat} [K]	923	923
T _{room} [K]	923	923
Layer [mm]	0.05	0.05
Beam Current [mA]	5	5
Beam Diameter[mm]	0.318	0.318
Acceleration Voltage[kV]	60	60
Heat Flux [W/mm ²]	788.56	788.56
v [mm/s]	450	650
Number of spots for the MultiBeam TM	70	70
Time-space between two subsequent jumping points for the MultiBeam TM [ms]	0.7	0.7

Table 2. Simulation inputs and process parameters for both MultiBeamTM and continuous line melting.

Both the width and the height of the cross-sections of the simulated melted lines were used for the comparison.

The samples were produced using an Arcam Q10 system with standard Arcam Ti6Al4V powder. The average of the particle size was 0.075 mm. The layer was fixed to 0.050 mm. The geometry of the samples was a parallelepiped with the length, the width and the height equal to 105 mm, 12.5 mm and 10 mm, respectively. On top of this geometry, additional single layer perimeters were melted. The dimensions of the perimeters are 5 mm x 10 mm and they are constituted by a single contour.

Each sample geometry has on the top 11 separate perimeters. The perimeters were melted with different process parameters. Figure 4 depicts one example of the produced samples.



Figure 4 Example of the produced samples

In [40], a light microscope was used to measure the width of the melted lines. For each side of the longer edges of the perimeter (C.f. figure 5-a, “right” and left”), seven widths were collected at distinct positions (Figure 5-b) to consider the actual line shape and its non-uniformity. In this work, the samples have been cut parallel to the longer side of the specimen and both the width and the height of the melted line have been measured on the cross-sections by light microscope as showed in Figure 5-c.

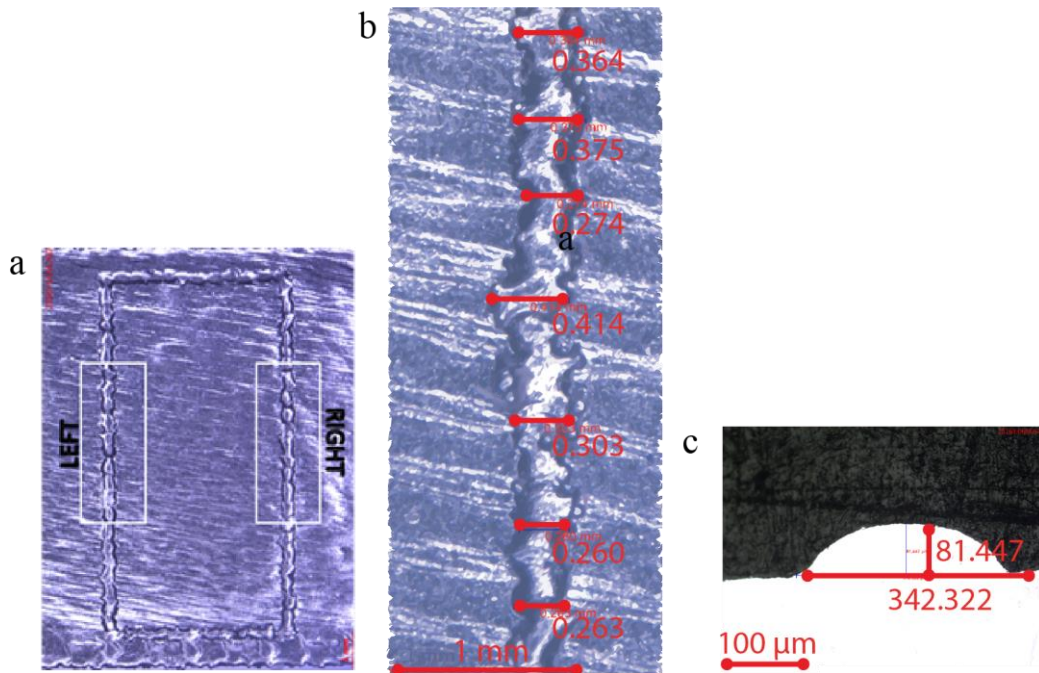


Figure 5 (a) An example of a microscope picture of the top view of a single perimeter; (b) magnification of one side of the perimeter and the measured widths; (c) cross-section of the melted line including measurements of width and height.

4. Result and Discussion

4.1 Cross-sections

Figure 6 and Figure 7 display experimental and numerical cross-sections of the MultiBeamTM and the continuous melted lines. The figures also show examples of top views of the experimentally melted lines. As can be seen, there are rather large variations of the cross-sections and of the form of the melted lines. In [40] the widths of the lines were measured at several points along the lines as in Figure 5. This approach was used for several lines melted with the same process settings, and a

detailed statistical analysis was performed. Below each top view in Figure 6 and Figure 7 the average values of the widths as obtained in [40] are included. These values are more representative measures than the rather few values obtained from the cross-sections. For practical reasons, similar statistical analysis as in [40] will not be possible for the cross-sections. However, the results from the cross-sections are believed to serve as good indicators of the melt track profiles and they provide useful information when comparing the experimental and the numerical results.

For MultiBeamTM (Figure 6) there is a variation in the cross-sections along the melt track that depends on the fractional melting of the line. The melted track consists of several short line segments that are equal to the beam speed times the spot time. Therefore, this melting strategy causes a variable melt pool geometry in which its cross-section, at the beginning of the short line, is smaller than at the end of the line. To account for the differences in the cross-sections, the numerical cross-sections have been collected at two different locations of the simulated line. The total length of the simulated line consisted of three multi beam line segments. The simulated cross-sections to the left in Figure 6 are close to the end of the second line segment whereas the ones to the right are obtained at the middle of the third line segment. When comparing the results between the calculated values and the simulated cross sections the model shows a good ability to predict the height of the melted line, while the width of the melted track is slightly underestimated. When comparing the average melt widths from [40] with the calculated melt widths the results are more similar.

As can be seen, there is a pronounced difference in height between the simulated cross-sections. This seems to be supported by the experimental results as well. However, it must be noted that the exact locations of the experimental cross-sections are not known. As will be discussed in Concluding Remarks a more detailed investigation of both experimental and simulated MultiBeamTM melting is planned. Here, the reason is assigned to the different cooling and heating sequences that take place. When the beam has melted one short line it jumps away and stays away for $69 \times 0.7 \text{ ms}$, which is the number of activated spots minus one multiplied by the time for each short line (spot time in Table 2). Then the beam comes back and starts to melt the subsequent line segment. For the higher speed, less line energy has been deposited. Thus, the underlying substrate has become less heated and therefore there are larger distortions. Since the beam jumps away there is no additional energy for relaxation as in the case of continuous line melting. Then, when the beam comes back to a position close to the point where there are large distortion different things could happen. If there is enough energy supplied, the distortion may relax, or re-melt, and the height may become lower. But if the energy is lower the distortion may become unaffected, or the increase in temperature may enhance the distortion and thus the height may become higher.

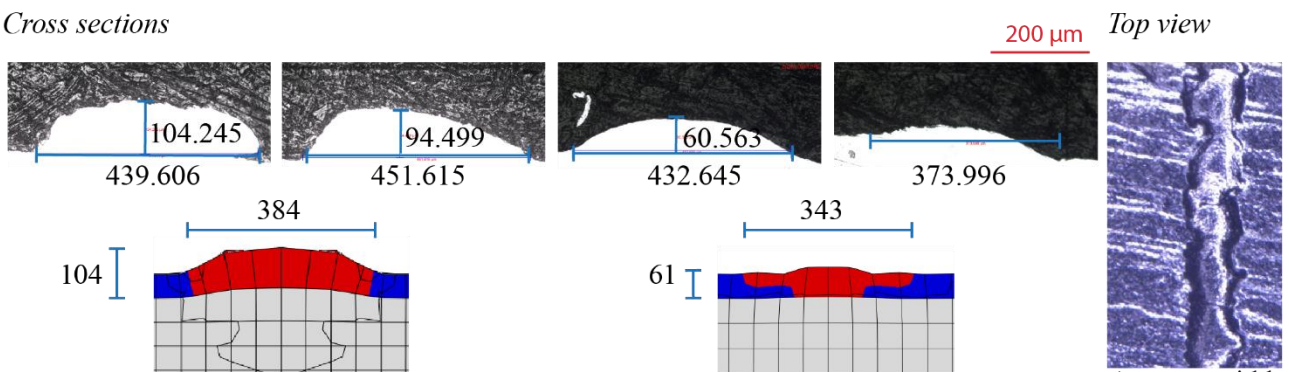
In the case of continuous line melting (Figure 7), the experimental cross sections for the higher speed are quite constant. For the same speed, the numerically melted line showed a cross-section that matches the experimental results rather well. However, the width of the line seems to be a bit overestimated when compared with the average value from [40].

For the lower value of the scan speed, the variations of the experimental cross-sections are rather drastic. The reason behind this phenomenon is not known. Presumably, these cross-sections indicate that there are variations in the powder layer thickness over the surface of the samples. However, the simulated height is in the same range as the average experimental height although the width seems to be overestimated. In this case, the simulated width compares well with the average value from [40].

The maximum deviation between the experimental and the numerical results was about 15% for the width and below 5% for the height of the melted line. When estimating the maximum deviation, the experimental cross-sections with a height lower than the layer thickness and a width smaller than the beam diameter (0.318mm) were excluded. The reason for excluding them is that they are not representative for lines melted with a layer thickness of 0.05 mm.

650 mm/s

Cross sections



450 mm/s

Cross sections

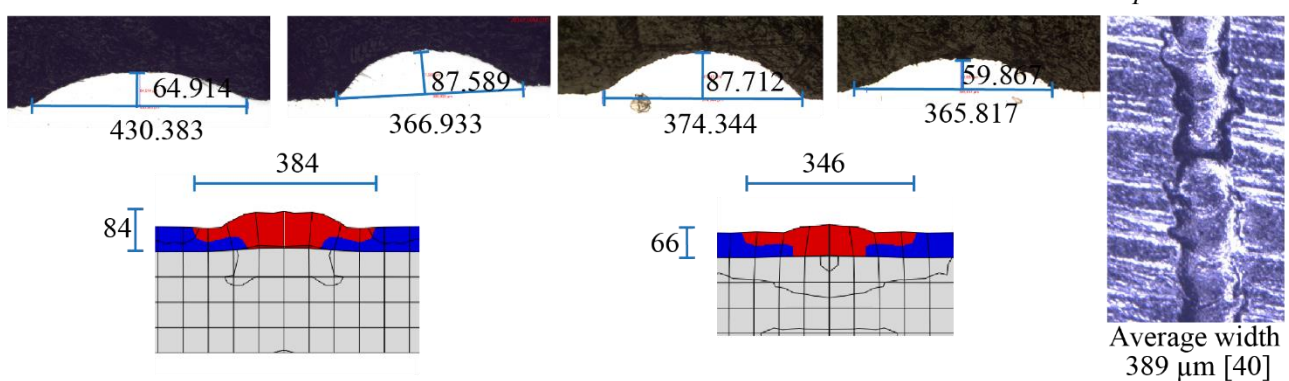
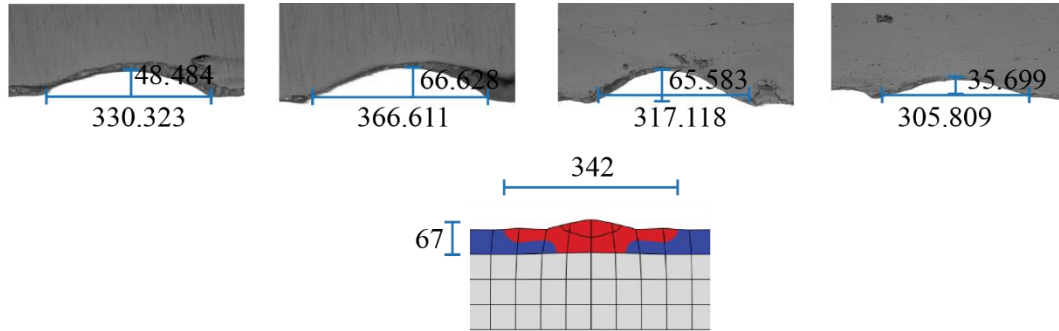


Figure 6 Experimental and numerical cross-sections in the case of MultiBeam™ melting. The values below the top views are the average melt widths obtained in [40].

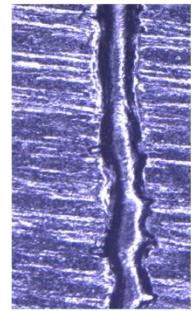
650 mm/s

Cross sections



200 μm

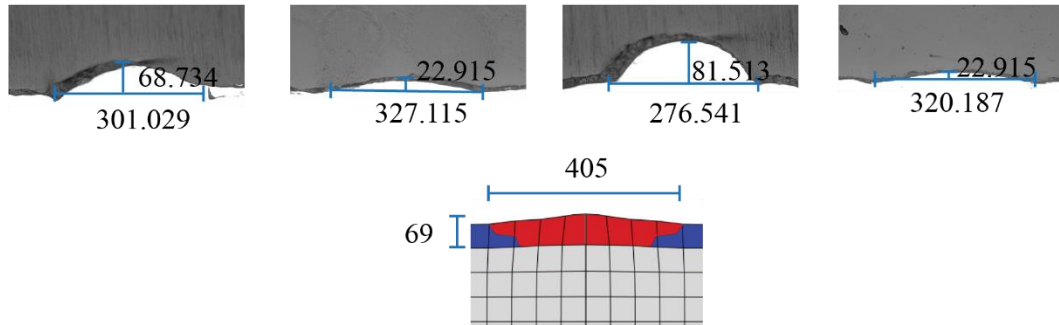
Top view



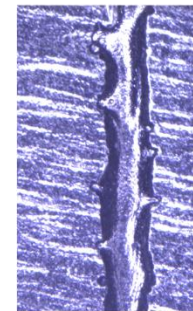
Average width
296 μm [40]

450 mm/s

Cross sections



Top view



Average width
402 μm [40]

Figure 7 Experimental and numerical cross-sections in the case of continuous line melting. The values below the top views are the average melt widths obtained in [40].

As a final comparison between experimental and simulated cross-sections the total melted area above the substrate is considered. Since the variation of the experimental cross-sections is rather large, the same cross-sections as used for estimating the maximum deviations for the widths and the heights were considered. The experimental and the simulated areas were measured in Illustrator CS6 Version 16.0.0 by cutting the image at the level of the substrate and then by calculating the number of pixels having a pixel value above a threshold. The measured areas are reported in Table 3.

Process Parameters	Experimental Area [10 ³ μm^2]	Numerical Area [10 ³ μm^2]
Multibeam		
650 mm/s	38.62	28.16
	31.18	13.87
	23.52	
450 mm/s	17.94	18.21
	21.68	14.38
	25.00	
	16.69	

Continuous		
650 mm/s	11.16	18.21
	12.84	
	10.03	
450 mm/s	14.71	18.67
	16.29	

Table 3. The total melted area above the substrate.

The deviations between the experimental and the numerical measurements of the areas are below 30% for the MultiBeamTM melted lines and below 15% for the continuous melted lines. These deviations are somewhat larger than the deviations obtained for the width and the heights. It is notable that the detected deviations are comparable to the area of a single particle. Thus, the deviations are at the margin of what can be expected, since dynamical effects such as absorption of particles into the melt volume [29, 41] are not accounted for in the model.

4.2 Comparison between thermal and thermomechanical models

The fact that the thermomechanical model captures geometrical changes that take place when melting the powder layer makes this model superior when comparing with the pure thermal model in [40]. However, it is interesting to compare the thermal response of the two models in detail to establish differences and underpinning causes. To do so the numerical results of continuous line melting were compared.

In Figure 8 the experimental and the calculated widths of the melted lines are displayed. The blue points represent the experimental measurements at 450 mm/s and 650 mm/s, respectively, while the red points are the corresponding averages. The black squares and triangles symbolize the numerical results for the thermomechanical and the pure thermal models, respectively. Numerically, for both models, MAT_ID was used to identify the width of the simulated melted line. The top views of the thermomechanical simulations are also displayed in Figure 8, overlapping the experimental results. As can be seen, the maximum deviation between experimental and numerical results is obtained for the thermal model for the line melted with 450 mm/s. This difference is outside the experimental error bars whereas the results obtained with the thermomechanical model are all within the variability of the experimental data. For 450 mm/s the thermomechanical model emulated a certain irregularity of the melted line width. This is due to the change of material properties that causes different shrinkages along the line. The irregularity is represented by a dispersion of the width of the simulated line (See the black interval bar in Figure 8). Similar irregularities were not observed with the thermal model for the same speed. For 650 mm/s the irregularity is within the melted zone and closer to the centre of the line (See the green area of the simulated line). Again, the pure thermal model did not display

the same effect. If there are similar thermal irregularities in the experimentally melted lines is not possible to view. Presumably, fluid dynamic effects will prevent such small geometric irregularities along the border of the melted line and maybe reduced thermal irregularities within the melt pool as well.

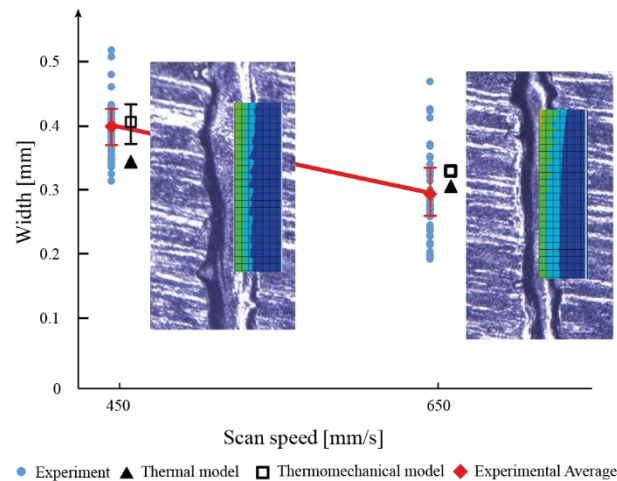


Figure 8 Comparison between experimental and calculated measures in the case of continuous line melting. Experimentally melted lines are displayed together with the results from the thermomechanical model.

The temperature distributions calculated with the two models are displayed in Figure 9. Below the liquidus temperature, the models provided quite similar results. However, above the liquidus temperature, the models predict somewhat different temperature distributions. This is due to the differences in heat transfer that arise as a result of the thermal expansion of the material.

Clearly, the thermomechanical model forecasts somewhat longer melt pool life and higher peak temperatures than the thermal model.

The longer melt pool life is explained by the amount of material behind the melt pool that has changed its state from powder (low conductivity) to solid (higher conductivity). For the thermomechanical model the changes in volume that are not present in the thermal model increase this amount of material, and since the material acts as a heat sink the lifetime of the melt pool will increase.

The higher temperature peak for the thermomechanical model is somewhat contradictory to the above explanation about the melt pool lifetime. Now, the higher peak is explained by a difference in heat transfer between the models at the front of the melt pool. For the thermomechanical model, the distance between two material points is temperature-dependent. Just in front of the melt pool, the distance between two points achieves the highest value. This is due to the high temperature and the large thermal gradient at the front, which produce a large expansion of the liquid and a shrinkage of the powder bed at the same time. Since there is no such increase in distance for the thermal model the thermal transfer will be lower for the thermomechanical model.

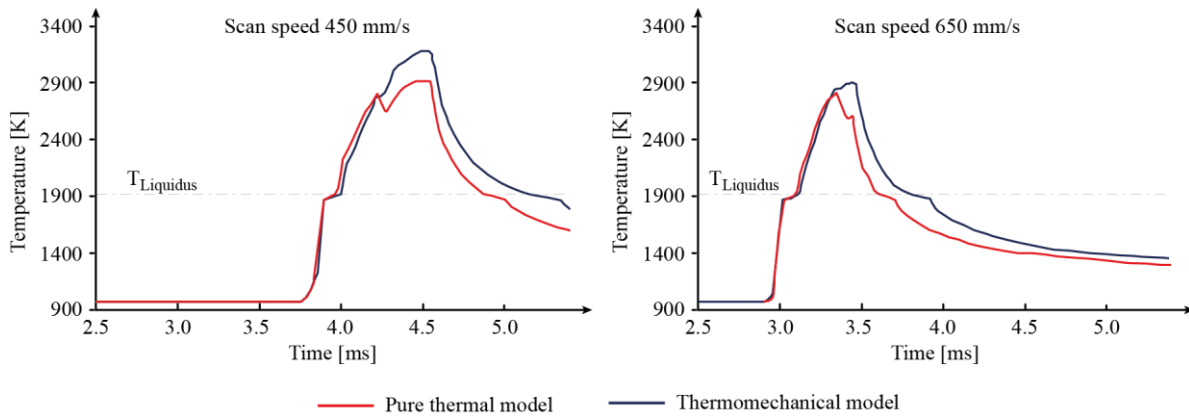


Figure 9 Comparison of the temperature profiles between the thermal and the thermomechanical models

In Figure 10 two sections of the melt pool along the melt lines are displayed. Although the maximum depths are rather similar for the two models, the depth profiles of the melt pool along the lines are rather different. This is due to the increased rate of the heat transfer caused by the volume change that in turn is caused by both the pseudo expansion coefficient and the expansion of the material properties during the melting and the cooling phases.

These thermal differences may be relevant when optimising the process parameters and the final microstructure of the material. In fact, a proper melt pool prediction could help to identify some quality issue such as the adhesion of the current layer with the previous one, the possible location of porosity and the total time for which a certain area is above a certain temperature. The latter will be important for understanding the evaporation of some alloy elements from the top surface and to understand the grain formation.

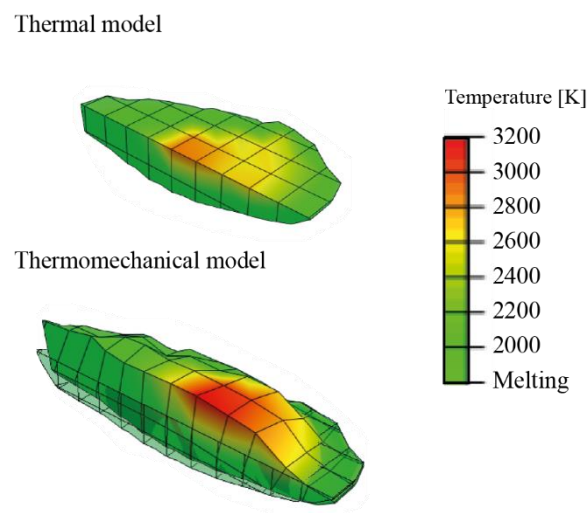


Figure 10 Section of the melt pools (Continuous line melting and scan speed equal to 650mm/s). The melt pool for the thermomechanical model is plotted on top off the undeformed melt pool.

4.3 Thermal stresses

Figure 11 (a) shows a portion of the cross-section of a melted line in which the total equivalent Von Mises thermal stress distribution during the beam passage is plotted. Along the line, the stress is zero in the melt pool, whereas higher stress levels can be observed in the solidified material close to the starting point. Stress gradients can also be observed at the interface between the melted line and substrate. In general, due to the high substrate temperature, the stresses are quite low. The star in Figure 11(a) indicates the location where the time evolution of temperature, material state variable (MAT_ID), displacement and thermal stresses have been collected. The results are plotted in Figure 11(b). According to the reference system (cf. Figure 11(a)), positive displacements indicate a shrinkage of the material and S11, S22 and S33 indicate the principal stresses along the X_1 , X_2 and X_3 axes, respectively. In the simulations, at the beginning and below the melting point, the temperature increase causes a shrinkage of the powder material while the stresses are almost zero. A further increase of the temperature up to the melting point of the material causes the material state to change from powder (MAT_ID=0) to bulk (MAT_ID=1). The material starts to expand. In this phase a low compressive stress state is present. After the beam passage and when the temperature drops below the melting point, the material shrinks and the stress level increases. Within the solidified material (below the melting temperature) there are only tensile contributions in the thermal stresses. Because of the high thermal gradients along the beam direction, the magnitude of the longitudinal component (S11) is higher than the transverse components. Presumably, these low residual stresses will be relaxed during the melting of the material adjacent to the melted line or during a post-heating phase.

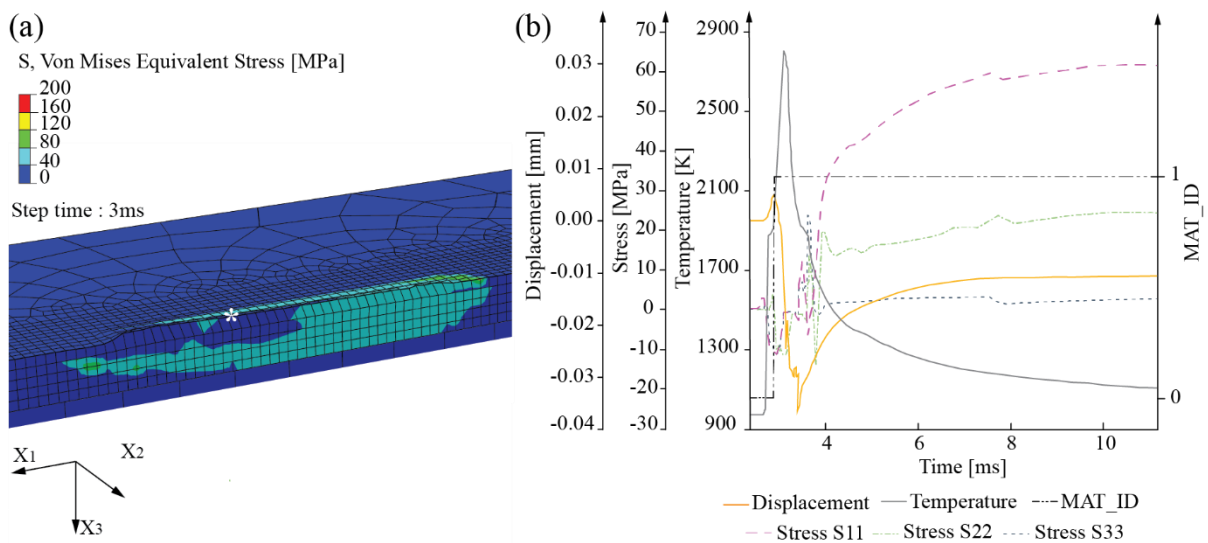


Figure 11 (a) Simulated equivalent stress (Von Mises) (b) Simulated displacement history, temperature history and thermal stresses histories close to the beam centre. The star on (a) indicates where the data were acquired. The process parameters are continuous strategy and scan speed equal to 650mm/s.

4.4 Computational considerations

The simulations have been performed on a personal computer equipped with an Intel® Core™ i7-6700K 4.00GHz processor and a 32GB RAM. Depending on the process parameters, the calculation times were typically between 1-3 minutes for each mm for the thermal model [40] and between 45-60 minutes for each mm for the thermomechanical model. A mesh convergence analysis was performed, and it was verified that a mesh size that balanced time and accuracy for the thermal model also could be used for the thermomechanical model. Finer meshes for the thermomechanical model caused little variation in displacement but increased the calculation time significantly. As an example, decreasing the mesh size from 0.05 mm to 0.025 mm increased the calculation time by a factor of 10. However, the maximum difference in displacement between the two meshes was less than 10 μm , and it was obtained directly at the beam passage point.

Since the main purpose of the presented work has been to evaluate the thermomechanical model, no further optimization measures were done to improve the performance of the calculations. It is expected that a better-adjusted mesh technique and an efficient implementation in a less general-purpose FE software will decrease the calculation time considerably.

5. Concluding remarks

In this work, a coupled thermo-mechanical model was developed to simulate single-line melt-track formations for Electron Beam Melting. The modelling considered the non-linear variations of the material properties when the material melts. New analytical formulations were introduced to account for physical aspects in both the powder layer and in the solid material. Particularly, the use of a pseudo thermal expansion was proposed to account both for thermal expansion of powder particles and for porosity reduction of the powder bed during the heating. Experimental and numerical results were compared both for continuous and MultiBeam™ line melting. The model appeared robust enough for providing consistent and valuable outputs for the different process settings.

The presented results demonstrate that the proposed approach will be an efficient model for simulating melt tracks in EBM. For instance, the results encourage further work on optimizing MultiBeam™ line melting as well as for understanding process variabilities. In a longer-term, even more ambitious applications might be considered such as: optimization of melted layer accuracy in terms of actual height and surface roughness, powder layer evolution during the preheating phase, possible location of microlocal stresses that can act as the nucleation of microcracks [42]. However, more detailed comparisons between experiments and simulations will clearly be needed to fully understand the applicability of the model.

Finally, it is suggested that the proposed approach might be useful for other powder-based AM processes as well, and hopefully this work will spark further developments of new and efficient models in the field.

References

- [1] M.S. J. Milberg, Electron Beam Sintering of metal powder, *Production Engineering* 2 (2008).
- [2] A. Mitchell, Melting, casting and forging problems in titanium alloys, *Materials Science and Engineering: A* 243(1) (1998) 257-262.
- [3] J. Parthasarathy, B. Starly, S. Raman, A. Christensen, Mechanical evaluation of porous titanium (Ti6Al4V) structures with electron beam melting (EBM), *Journal of the mechanical behavior of biomedical materials* 3(3) (2010) 249-259.
- [4] O.L. Harrysson, O. Cansizoglu, D.J. Marcellin-Little, D.R. Cormier, H.A. West, Direct metal fabrication of titanium implants with tailored materials and mechanical properties using electron beam melting technology, *Materials Science and Engineering: C* 28(3) (2008) 366-373.
- [5] P. Heini, C. Körner, R.F. Singer, Selective electron beam melting of cellular titanium: mechanical properties, *Adv Eng Mater* 10(9) (2008) 882-888.
- [6] S. Fager Franzén, J. Karlsson, Titanium Aluminide Manufactured by Electron Beam Melting, (2010).
- [7] S. Biamino, A. Penna, U. Ackelid, S. Sabbadini, O. Tassa, P. Fino, M. Pavese, P. Gennaro, C. Badini, Electron beam melting of Ti-48Al-2Cr-2Nb alloy: Microstructure and mechanical properties investigation, *Intermetallics* 19(6) (2011) 776-781.
- [8] I. Gibson, D.W. Rosen, B. Stucker, *Additive manufacturing technologies*, Springer 2010.
- [9] L.E. Murr, E. Martinez, K.N. Amato, S.M. Gaytan, J. Hernandez, D.A. Ramirez, P.W. Shindo, F. Medina, R.B. Wicker, Fabrication of metal and alloy components by additive manufacturing: examples of 3D materials science, *Journal of Materials Research and technology* 1(1) (2012) 42-54.
- [10] M. Galati, L. Iuliano, A literature review of powder-based electron beam melting focusing on numerical simulations, *Additive Manufacturing* 19 (2018) 1-20.
- [11] J. Karlsson, T. Sjögren, A. Snis, H. Engqvist, J. Lausmaa, Digital image correlation analysis of local strain fields on Ti6Al4V manufactured by electron beam melting, *Materials Science and Engineering: A* 618 (2014) 456-461.
- [12] S. Tammas-Williams, H. Zhao, F. Leonard, F. Derguti, I. Todd, P.B. Prangnell, XCT analysis of the influence of melt strategies on defect population in Ti-6Al-4V components manufactured by Selective Electron Beam Melting, *Mater Charact* 102 (2015) 47-61.
- [13] T. Mahale, *Electron Beam Melting of Advanced Materials and Structures, mass customization, mass personalization*, North Carolina State University, Raleigh, NC., 2009.
- [14] W.W. He, W.P. Jia, H.Y. Liu, H.P. Tang, X.T. Kang, Y. Huang, Research on Preheating of Titanium Alloy Powder in Electron Beam Melting Technology, *Rare Metal Mat Eng* 40(12) (2011) 2072-2075.
- [15] F. Calignano, M. Galati, L. Iuliano, P. Minetola, Design of Additively Manufactured Structures for Biomedical Applications: A Review of the Additive Manufacturing Processes Applied to the Biomedical Sector, *Journal of healthcare engineering* 2019 (2019).
- [16] F. Froes, B. Dutta, The additive manufacturing (AM) of titanium alloys, *Advanced Materials Research, Trans Tech Publ*, 2014, pp. 19-25.
- [17] V. Juechter, T. Scharowsky, R. Singer, C. Körner, Processing window and evaporation phenomena for Ti-6Al-4V produced by selective electron beam melting, *Acta Materialia* 76 (2014) 252-258.
- [18] H. Qi, Y. Yan, F. Lin, R. Zhang, Scanning method of filling lines in electron beam selective melting, *Proceedings of the Institution of Mechanical Engineers, Part B: Journal of Engineering Manufacture* 221(12) (2007) 1685-1694.
- [19] M.F. Zäh, S. Lutzmann, Modelling and simulation of electron beam melting, *Production Engineering* 4(1) (2010) 15-23.
- [20] N. Shen, K. Chou, Thermal Modeling of Electron Beam Additive Manufacturing Process: Powder Sintering Effects, *ASME 2012 International Manufacturing Science and Engineering Conference collocated with the*

40th North American Manufacturing Research Conference and in participation with the International Conference on Tribology Materials and Processing, American Society of Mechanical Engineers, 2012, pp. 287-295.

[21] B. Cheng, K. Chou, Melt pool geometry simulations for powder-based electron beam additive manufacturing, 24th Annual International Solid Freeform Fabrication Symposium-An Additive Manufacturing Conference, Austin, TX, USA, 2013.

[22] B. Cheng, S. Price, X. Gong, J. Lydon, K. Cooper, K. Chou, Speed Function Effects in Electron Beam Additive Manufacturing, ASME 2014 International Mechanical Engineering Congress and Exposition, American Society of Mechanical Engineers, 2014, pp. V02AT02A003-V02AT02A003.

[23] N. Shen, Y. Chou, Numerical thermal analysis in electron beam additive manufacturing with preheating effects, Proceedings of the 23rd Solid Freeform Fabrication Symposium, Austin, TX, 2012, pp. 774-784.

[24] B. Cheng, S. Price, J. Lydon, K. Cooper, K. Chou, On Process Temperature in Powder-Bed Electron Beam Additive Manufacturing: Model Development and Validation, J Manuf Sci E-T Asme 136(6) (2014).

[25] D. Riedlbauer, T. Scharowsky, R.F. Singer, P. Steinmann, C. Körner, J. Mergheim, Macroscopic simulation and experimental measurement of melt pool characteristics in selective electron beam melting of Ti-6Al-4V, The International Journal of Advanced Manufacturing Technology (2016) 1-9.

[26] D. Riedlbauer, P. Steinmann, J. Mergheim, Thermomechanical finite element simulations of selective electron beam melting processes: performance considerations, Computational Mechanics 54(1) (2014) 109-122.

[27] B. Cheng, P. Lu, K. Chou, Thermomechanical investigation of overhang fabrications in electron beam additive manufacturing, ASME 2014 International Manufacturing Science and Engineering Conference collocated with the JSME 2014 International Conference on Materials and Processing and the 42nd North American Manufacturing Research Conference, American Society of Mechanical Engineers, 2014, pp. V002T02A024-V002T02A024.

[28] N. Shen, K. Chou, Simulations of thermo-mechanical characteristics in electron beam additive manufacturing, ASME 2012 International Mechanical Engineering Congress and Exposition, American Society of Mechanical Engineers, 2012, pp. 67-74.

[29] M. Galati, L. Iuliano, A. Salmi, E. Atzeni, Modelling energy source and powder properties for the development of a thermal FE model of the EBM additive manufacturing process, Additive Manufacturing 14 (2017) 49-59.

[30] S.S. Sih, J.W. Barlow, Emissivity of powder beds, Solid Freeform Fabrication Symposium Proceedings, Center for Materials Science and Engineering, Mechanical Engineering Department and Chemical Engineering Department, the University of Texas at Austin, 1995, pp. 7-9.

[31] N.K. Tolochko, M.K. Arshinov, A.V. Gusarov, V.I. Titov, T. Laoui, L. Froyen, Mechanisms of selective laser sintering and heat transfer in Ti powder, Rapid Prototyping Journal 9(5) (2003) 314-326.

[32] R.M. German, Particle Packing Characteristics, Metal Powder Industries Federation 1989.

[33] A.R. Khoei, Numerical simulation of powder compaction processes using an inelastic finite element analysis, Materials & design 23(6) (2002) 523-529.

[34] M. Matsumoto, M. Shiomi, K. Osakada, F. Abe, Finite element analysis of single layer forming on metallic powder bed in rapid prototyping by selective laser processing, International Journal of Machine Tools and Manufacture 42(1) (2002) 61-67.

[35] L. Parry, I. Ashcroft, R.D. Wildman, Understanding the effect of laser scan strategy on residual stress in selective laser melting through thermo-mechanical simulation, Additive Manufacturing 12 (2016) 1-15.

[36] Abaqus, ABAQUS Documentation, Dassault Systèmes, Providence (USA), 2014.

[37] M. Boivineau, C. Cagran, D. Doytier, V. Eyraud, M.-H. Nadal, B. Wilthan, G. Pottlacher, Thermophysical properties of solid and liquid Ti-6Al-4V (TA6V) alloy, International journal of thermophysics 27(2) (2006) 507-529.

[38] D. Basak, R.A. Overfelt, D. Wang, Measurement of specific heat capacity and electrical resistivity of industrial alloys using pulse heating techniques, International Journal of Thermophysics 24(6) (2003) 1721-1733.

[39] Z. Guo, N. Saunders, J. Schillé, A. Miodownik, Modelling high temperature flow stress curves of titanium alloys, MRS International Materials Research Conference, 2008, pp. 9-12.

- [40] M. Galati, A. Snis, L. Iuliano, Experimental validation of a numerical thermal model of the EBM process for Ti6Al4V, *Computers & Mathematics with Applications* (2018).
- [41] O. Cansizoglu, O. Harrysson, D. Cormier, H. West, T. Mahale, Properties of Ti–6Al–4V non-stochastic lattice structures fabricated via electron beam melting, *Materials Science and Engineering: A* 492(1-2) (2008) 468-474.
- [42] R.I. Stephens, A. Fatemi, R.R. Stephens, H.O. Fuchs, *Metal fatigue in engineering*, John Wiley & Sons 2000.